OPEN ACCESS

Japanese Journal of Applied Physics **63**, 065003 (2024) **REGULAR PAPER**

https://doi.org/**10.35848/1347-4065/ad53b1**

Thermal-aware device design of low-power H_2S sensors using Joule-heated Au nanosheet

Taro Kato[1*], Takahisa Tanaka[2], and Ken Uchida[1*]

[1]*Department of Materials Engineering, The University of Tokyo, Bunkyo, Tokyo 113-8656, Japan*
[2]*Department of Electronics and Electrical Engineering, Keio University, Hiyoshi, Yokohama 223-8522, Japan*

[*]E-mail: kato@ssn.t.u-tokyo.ac.jp; uchidak@material.t.u-tokyo.ac.jp

Received February 9, 2024; revised May 23, 2024; accepted June 2, 2024; published online June 25, 2024

We demonstrated Joule-heated Au nanosheet H_2S sensors for low-power operation. We confirmed that low temperature regions in the Joule-heated Au nanosheet caused lower response and recovery characteristics than uniformly heated Au nanosheets. By using Pt electrodes, which has lower thermal conductivity than Au, heat dissipation to the electrodes could be suppressed, resulting in lower power consumption and faster recovery characteristics. We then discussed the optimal sensor structure by developing an analytical model of electrical and thermal resistances. We introduced semi-elliptical intermediate electrodes between the channel and pad electrodes to efficiently suppress the heat dissipation, demonstrating that the optimal channel length and thermal conductivity of the intermediate electrode κ_{int} exist depending on the channel width. Finally, we proposed the sensor design strategy of considering the κ_{int} dependences of the electrical and thermal resistances. This strategy is useful for all metal nanosheet sensors because it gives an estimation of their optimal structures. © 2024 The Author(s). Published on behalf of The Japan Society of Applied Physics by IOP Publishing Ltd

1. Introduction

Demands of low-power and small-size gas sensors are increasing in the Internet-of-Things (IoT) society. These gas sensors are expected to enable safety verification of hydrogen fuel[1)] and solid-state batteries,[2)] health checkups based on breath analysis,[3,4)] and process management in factories and farms.[5,6)] However, it is difficult for existing commercial gas sensors to realize such ubiquitous sensing. Metal oxide semiconductor (MOS) gas sensors, which are most widely-used methods, have challenges in power consumption because they need to be heated to high temperatures to obtain chemical reactions.[3,7)] Electrochemical (EC) gas sensors are also widely commercialized. However, these gas sensors using liquid electrolytes are difficult to miniaturize because they require bulky cell structures to seal the electrolytes within gas permeable membranes.[8)] Although MOS sensors that operate at room temperature using catalytic materials[7,9,10)] and miniaturized EC sensors using ionic-liquid[11,12)] have been proposed to meet these demands in the IoT society, these sensors still have challenges in response and recovery speed.

Joule-heating is attracting attention as a low-power method for gas sensors using MOS nanowires[13,14)] and other conductive nanoscale materials such as carbon nanotubes (CNT),[15)] graphenes,[16,17)] and metal nanosheets.[18,19)] By using Joule heat generated by high current density through a conductive material, only the sensing part can be locally heated, which is much more efficient than an external heater that heats the entire substrate. In addition, Joule heating is advantageous for sensor integration because the multiple sensors can be adjusted to the optimum temperatures for each device by changing the applied voltage for each device and target gas.[16,20)]

Here, we focused on metal nanosheet gas sensors,[21)] where chemisorbed molecules change their resistances by inducing diffusive electron scatterings at their surfaces,[22,23)] as shown in Fig. 1. Since metal nanosheet gas sensors can be fabricated via simple lithographic processes, they can be easily miniaturized, which is advantageous for Joule heating with low power consumption.[20)] We chose gold (Au) as the sensing material and hydrogen sulfide (H_2S) as the target gas.[24,25)] Several papers have applied Joule heating to Au nanosheets to investigate electromigration of interconnects and heat conduction in nanoscale metals.[26–29)] However, to the best of our knowledge, there are few reports on the application of Joule-heated Au nanosheets to H_2S sensors.

In the extended abstract of the 2023 International Conference of Solid State Devices and Materials: SSDM2023, we demonstrated that Au nanosheets can detect H_2S with low power by using Joule heating.[30)] On the other hand, we confirmed that heat dissipation to the electrodes and the large temperature gradient in the Joule-heated Au nanosheet caused power loss and poorer sensor response/recovery characteristics than uniformly heated Au nanosheets. In this paper, in addition to the experimental results reported in SSDM2023, we discuss a device structure that enables Joule heating efficiently by applying thermal-aware design for nanosheets and electrodes. We introduce the semi-elliptical intermediate electrode structure between the channel and the pad electrodes into an existing analytical model to most efficiently suppress the heat dissipation. This analytical model suggests that there are the optimal channel length L_{ch} and thermal conductivity of the intermediate electrode κ_{int} depending on the channel width W_{ch}. Based on these suggestions, we propose the sensor design strategy of considering the κ_{int} dependences of the electrical and thermal resistances. Our analytical model proposed in this study is applicable to other metal nanosheet sensors, and we expect that the sensor design strategy is useful for other nanostructured sensors (CNTs, graphenes, and MOS nanowires).

2. Experimental methods

2.1. Device fabrication

We deposited a 16 nm thick Au nanosheet with a 2 nm thich titanium nitride (TiN) adhesion layer on a Si substrate with a

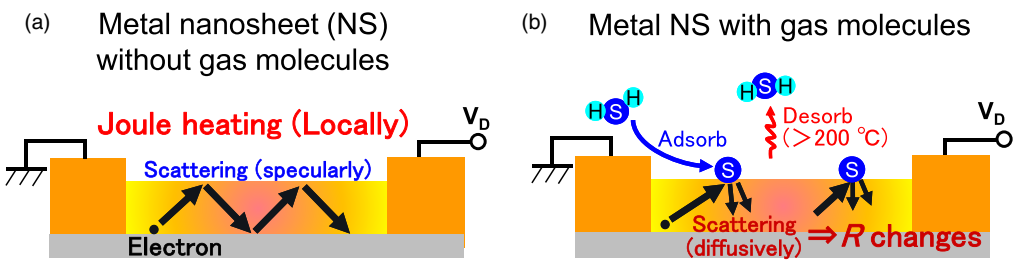

Fig. 1. Schematics of Joule-heated metal nanosheet gas sensors. (a) Electrons scatter specularly at the metal surface without gas molecules. (b) Electron scattering turns diffusive when gas molecules absorb on the surface, resulting in resistance increases.

1 μm thick thermally grown SiO_2 layer. The Au and TiN layers were deposited by RF sputtering (CFS-4ES, Shibaura) at a base pressure of 8.4×10^{-4} Pa and a chamber pressure of 0.44 Pa, which were adjusted using an Ar flow. The deposited Au nanosheet was annealed in a N_2 atmosphere at 300 °C for 1 h to improve its crystallinity. The Au nanosheet and the electrode was patterned by using electron-beam (EB) lithography (F7000S-VD02, Advantest Co.). After the patterning, 60 nm thick Au electrodes along with a 5 nm thick Cr adhesion layer or 18 nm thick Pt electrodes were fabricated through a lift-off process using the same EB lithography system.

Figure 2(a) presents the scanning electron microscopy (SEM) image of the Au nanosheet, indicating that the Au nanosheet with a uniform width of approximately 400 nm was properly formed. Figure 2(b) presents the cross-sectional TEM image of the Au nanosheet, indicating that the flat Au nanosheet with the thickness of approximately 16 nm along with the 2 nm thick TiN adhesion layer was successfully formed on the SiO_2/Si substrate.

2.2. Gas-sensing setup

We used dry air as the base gas to measure the gas-sensing properties. The concentration of the target gas (H_2S) was controlled by mixing gases whose flow rate at 400 sccm was controlled using flowmeters. We applied a constant current using a current source (6221, Keithley) and obtained the nanosheet resistance by measuring the voltage using a digital multimeter (2000, Keithley). The temperature of the sensor was controlled using an external heater in conjunction with a thermocouple. The sensor response was represented by target-gas-induced resistance changes normalized by the original resistance $\Delta R/R_0$ (%), where R_0 represents the resistance of the sensor during dry air flow and ΔR represents the resistance change by H_2S (target gas) exposure.

3. Results and discussion

3.1. Gas-sensing characteristics

Figure 3(a) shows the responses of the Au nanosheet sensor with the 60 nm thick Au electrodes heated by the external heater and by Joule heating. The sensor was exposed to H_2S gas at a concentration of 4.5 ppm for 30 s. The channel width and length of the Au nanosheet were 400 nm and 2 μm, respectively. Since H_2S molecules adsorb and desorb frequently at the temperatures of higher than 200 °C,[24] the power of 2.5 mW for Joule heating was applied for realizing the nanosheet temperatures of sufficiently higher than 200 °C. The maximum response of the Au nanosheet sensor heated by Joule heating (3.8%) was about the half of that heated by the external heater (8.1%). We considered that the smaller sensor response was due to the non-uniform temperature profile in the Au nanosheet channel during the Joule heating. Figure 3(b) shows the temperature distribution of the Joule-heated Au nanosheet with the Au electrodes simulated by a finite-element method (FEM) using COMSOL Multiphysics©, and Fig. 3(c) presents the one-dimensional temperature profile along the channel. These results clearly indicated that the temperatures at the edges of the channel were well below 200 °C. Since the thermal conductivity of Au is so large (κ: 318 $W \cdot m^{-1} \cdot K^{-1}$) that the large amount of the Joule heat generated in the channel dissipated into the Au electrodes, resulting in the temperature drops in the channel near the electrodes. We considered that the low temperature regions in the channel were responsible for the smaller sensor response. Since the low temperature regions could also cause the poor recovery characteristics, it is strongly desired for the Joule-heated Au nanosheet sensors to raise the entire channel temperatures to higher than 200 °C.

In order to realize the uniformly Joule-heated Au nanosheet, we then adopted a Au nanosheet with a long channel length. Figure 4(a) shows the simulation result of the one-dimensional temperature profile in the Joule-heated Au nanosheet with the channel width of 800 nm and the channel length of 80 μm. For a nanosheet with a sufficiently long channel, heat dissipation to the substrate is much more dominant than that to the electrodes.[13] Since only the heat dissipation to the substrate occurs in the central region of the long channel, the temperature is uniform in this region. Hence, the temperatures of about 90% of the channel regions

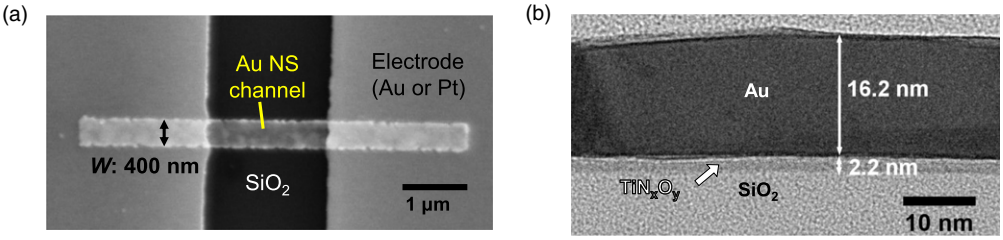

Fig. 2. (a) SEM image of Au nanosheet with electrodes. (b) Cross-sectional TEM image of Au nanosheet.

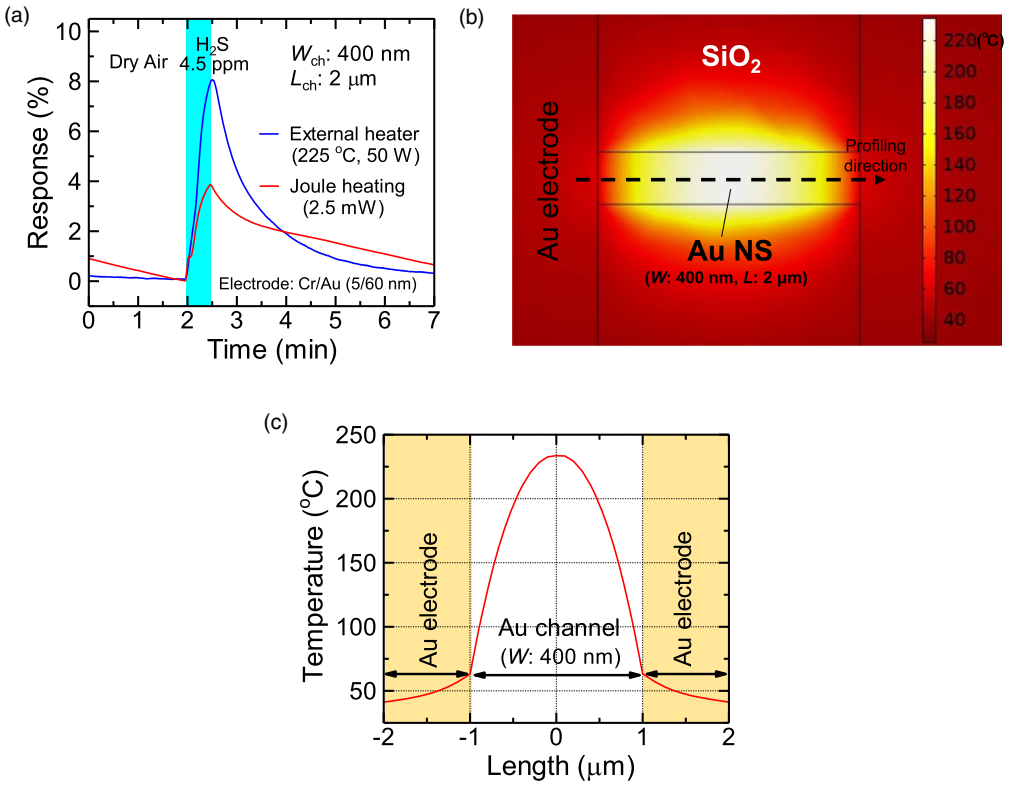

Fig. 3. (a) Responses of the Au nanosheet sensor with the Au electrodes to 4.5 ppm H_2S heated by the external heater (blue) and by Joule heating (red line). (b) Simulated temperature profile of the Joule-heated Au nanosheet sensor and (c) one-dimensional temperature profile.

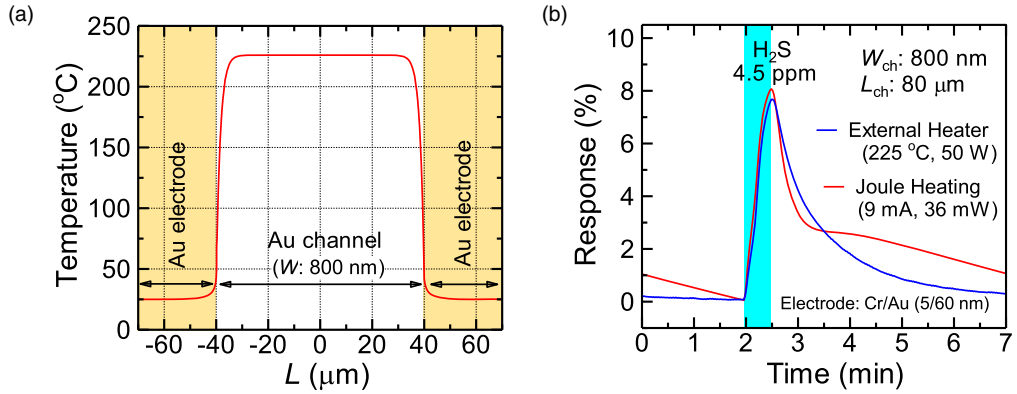

Fig. 4. (a) Simulation result of one-dimensional temperature profile of Joule-heated long-channel Au nanosheet. (b) Sensor responses of long-channel Au nanosheet heated by external heater (blue line) and by Joule heating (red line).

were uniform and higher than 200 °C in Fig. 4(a). Figure 4(b) presents the responses of the Joule-heated Au nanosheet heated by the external heater and heated by Joule heating. The Au nanosheet was exposed to 4.5 ppm H_2S for 30 s. Although the power consumption was 36 mW, the long-channel Joule-heated Au nanosheet exhibited almost the same magnitude of the sensor response as that heated by the external heater. This result suggested that small temperature drops near the channel edges are pivotal for highly sensitive Joule-heated Au nanosheet sensors, whereas a short channel is necessary for low-power operation.

Suppressing the heat dissipation to the electrodes is required to reduce the temperature drops in a short-channel Au nanosheet. We changed the electrode material from Au to Platinum (Pt) because the thermal conductivity of Pt (κ: 71 $W \cdot m^{-1} \cdot K^{-1}$) is much lower than that of Au (κ: 318 $W \cdot m^{-1} \cdot K^{-1}$). Figure 5(a) shows the simulation result of the temperature distribution in the Joule-heated Au nanosheet with the 18 nm thick Pt electrodes, suggesting that the Joule heat is localized within the Au nanosheet channel thanks to the lower thermal conductivity of the Pt electrodes. Figure 5(b) compared the simulated temperature profiles of the Au nanosheet with the 18 nm thick Pt electrodes and with the 60 nm thick Au electrodes. Here, the red line in Fig. 5(b) is the same result as that in Fig. 3(c). The temperature drops in the Au nanosheet with 18 nm thick Pt electrodes were much smaller than that in the Au nanosheet with 60 nm thick Au electrodes. Figure 5(c) shows the sensor responses of the Au nanosheet with Pt electrodes to 4.5 ppm H_2S. Although the sensor response was smaller (3.5%) because of the larger resistance of the Pt electrodes, the Joule-heated Au nanosheet with the power of 1.7 mW showed almost the same sensor response to that heated by the external heater. Therefore, we concluded that low-power and highly sensitive Au nanosheet

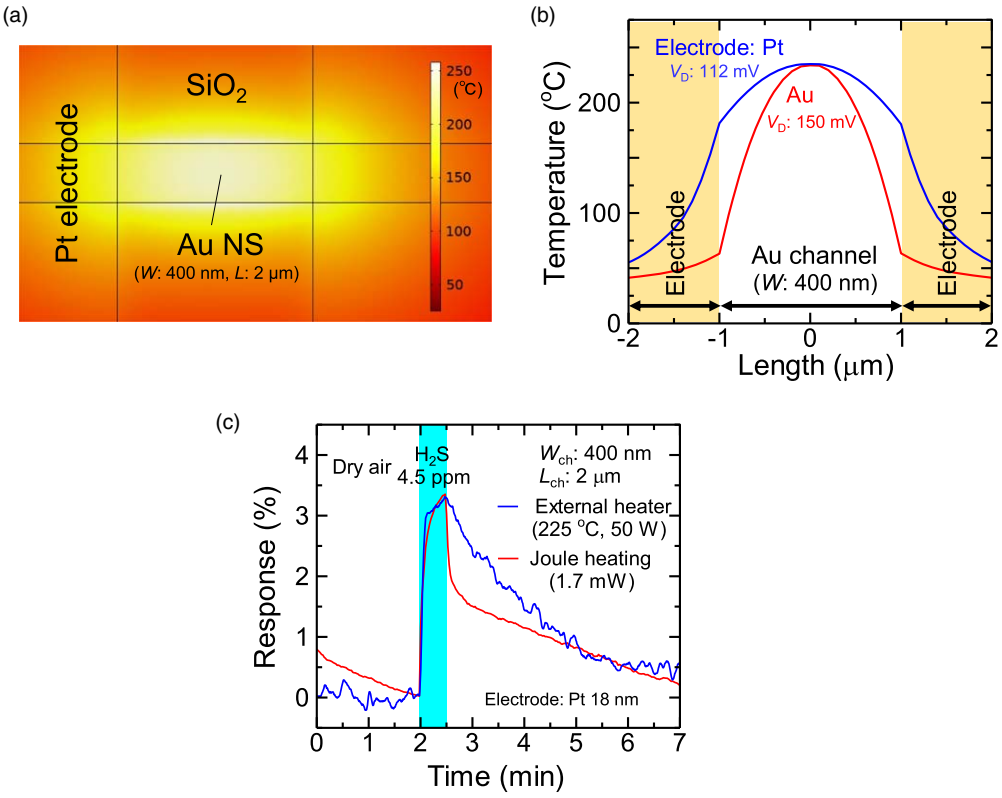

Fig. 5. (a) Simulated temperature profile of Joule-heated Au nanosheet with Pt electrodes. (b) Comparison of temperature profiles of Au nanosheets with 60 nm thick Au electrodes (red line) and 18 nm thick Pt electrodes (blue line). (c) Sensor responses of Au nanosheet with Pt electrodes heated by external heater (blue line) and by Joule heating (red line).

H_2S sensor was realized by introducing Pt, a lower thermal conductivity material than Au, as the electrodes.

3.2. Optimization of structure of Joule-heated metal nanosheet

In order to optimize the device structure of the Joule-heated Au nanosheet, we developed an analytical model of the temperature distribution and the electrical resistances.

3.2.1. Existing analytical model. To investigate thermal-aware device structures, we utilized Hunley's analytical model for calculating temperature distribution,[31] which has been developed based on a simple device structure including a nanosheet and semi-infinite length electrodes. Their analytical model can give the estimation of the temperature distribution in the Joule-heated metal nanosheet in good agreement with the FEM results by accurately describing heat dissipation into the substrate and the electrodes. In their model, the one-dimensional temperature profiles inside the metal nanosheet and the electrodes are given as follows:

$$\Delta T(x) = 2A\cosh(m_1 x) + \frac{Q}{\kappa_{ch} m_1^2} \quad \text{for} \quad |x| \leqslant L_{ch}/2 \tag{1}$$

$$\Delta T(x) = BK_0\left(m_2\left(|x| - \frac{L_{ch}}{2} + \frac{W_{ch}}{2+\pi}e^{-2(|x|-L_{ch}/2)/W_{ch}}\right)\right) \quad \text{for} \quad L_{ch}/2 < |x| \leqslant W_{int}/2 \tag{2}$$

$$\Delta T(x) = Ce^{-m_2\left(|x|-\frac{W_{int}}{2}\right)} \quad \text{for} \quad W_{int}/2 \leqslant \pm x \tag{3}$$

where L_{ch} and W_{ch} are the channel length and width of the nanosheet, κ_{ch} is the thermal conductivity of the nanosheet, W_{int} is the width of the electrode. K_0 in Eq. (2) is the modified Bessel function of the second kind of order zero, and m_1 and m_2 are the reciprocals of the thermal healing lengths along the nanowire and the electrodes, expressed by the following equations:

$$m_1^2 = \frac{\kappa_{sub}\pi}{W_{ch}t_{ch}\kappa_{ch}\ln\left(\frac{d}{W_{ch}}(2+\pi) + e^{-\frac{2d}{W_{ch}}}\right)} \tag{4}$$

$$m_2^2 = \frac{\kappa_{sub}}{\kappa_{int}t_{int}d}, \tag{5}$$

where κ_{int} and κ_{sub} are the thermal conductivity of the electrodes and the substrate, t_{ch}, t_{int}, t_{sub} are the thicknesses of the nanosheet, the electrodes, and the substrate, respectively. Finally, constant A, B, C in Eqs. (1)–(3) are obtained by solving the boundary conditions of equal temperatures at the boundaries and the continuity of the heat flow.

3.2.2. Introducing intermediate electrode structure into the analytical model. We can calculate the temperature distribution in the metal nanosheet using Hunley's model. However, we cannot calculate the power consumption because the electrodes with semi-infinite lengths are considered in Hunley's model, and the electrical resistances of the electrodes cannot be defined. Then, we newly introduced intermediate electrode structures between the channel and the pad electrodes into the Hunley's analytical model to calculate their resistances. Figure 6 shows the schematic of the metal

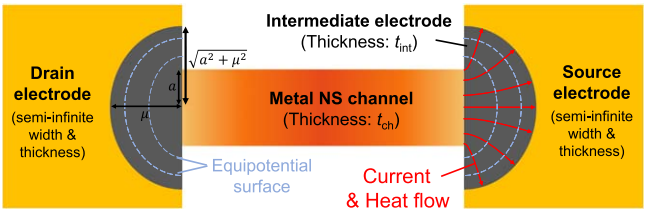

Fig. 6. Schematic of metal nanosheet with intermediate electrodes.

nanosheet with the intermediate electrodes. As described in Appendix A, the equipotential surfaces from the channel edge are semi-elliptical in shape. Because the temperature distribution in the intermediate electrode region is also expected to be semi-elliptical in shape, we set the intermediate electrode structure as a semi-ellipse to localize the Joule heat while suppressing its electrical resistance. Here, the length of the intermediate electrode μ in the channel length direction should be comparable to the thermal healing length $1/m_2$ to most effectively localize the Joule heat in the channel.

In the metal nanosheet device as shown in Fig. 6, the total resistance is the sum of the channel resistance R_{ch} and the intermediate electrode resistances $2R_{int}$. Here, the pad electrodes are assumed to be semi-infinitely large, and their electrical resistances are considered to be zero. R_{ch} can be written as

$$R_{ch} = \frac{1}{W_{ch}\ t_{ch}} \int_{-\frac{L_{ch}}{2}}^{\frac{L_{ch}}{2}} \rho_{ch}(T)\ dl. \tag{6}$$

As for R_{int}, the capacitance between two elliptical conductors is defined by Eq. (B·3) in Appendix B. The equation relating the capacitance and resistance between two equipotential surfaces in an arbitrary geometry is described by Holm as follows:[32]

$$R_{c1} = \frac{|\varphi_c - \varphi_1|}{I} = \frac{\varepsilon_0 \rho}{C}. \tag{7}$$

Thus, when the electrical resistivity ρ_{int} is constant, R_{int} is obtained from Eqs. (B·3) and (7) as

$$R_{int} = \frac{\rho_{int}}{\pi t_{int}} \log\left(\frac{\sqrt{W_{ch}^2/4 + \mu^2} + \mu}{W_{ch}/2}\right). \tag{8}$$

The temperature of the intermediate electrodes also rise during the Joule heating operation. The change in R_{int} due to the rise in the temperature (ΔT_{int}) was taken into consideration by averaging the temperature rise at each location over the entire intermediate electrode region.

3.2.3. Calculation conditions. Using Hunley's analytical model, Eqs. (6), and (8), we calculated the temperature distribution and electrical resistance of the Joule-heated Au nanosheet with the intermediate electrodes. Details of the calculation conditions in this study are listed below:

(i) In a Au nanosheet sensor, fast response/recovery can be achieved when the entire channel is heated to 200 °C or higher, as shown in Fig. 5. Therefore, all the calculations were performed on the condition that an ambient temperature was 25 °C and a channel edge temperature reached 200 °C by Joule heating.

(ii) As for the length of the intermediate electrode $\mu = L_{int}$ required for the thermal localization, the temperature in the intermediate electrode region decays according to the the modified Bessel function K_0 [Eq. (2)]. Since this modified Bessel function decreases exponentially as x increases, we determined L_{int} as the distance at which the temperature decays to $+175$ $(=200–25)/e^3 \simeq +8.71$ °C.

(iii) Heat dissipation by convection and by radiation was not considered.

(iv) Since the thermal conductivities of Au and Pt by phonons are significantly lower (Au: $\sim 2\ \mathrm{W \cdot m^{-1} \cdot K^{-1}}$, Pt: $\sim 6\ \mathrm{W \cdot m^{-1} \cdot K^{-1}}$) than those by electrons,[33,34] thermal transport by phonons was not considered.

(v) The electrical and thermal conductivities of the intermediate electrode σ_{int} and κ_{int} were defined based on the Wiedemann–Franz law ($\kappa/\sigma = L/T$, L: Lorenz number).

(vi) t_{ch} and t_{int} were set to be the same ($t_{ch} = t_{int}$).

3.3. Calculation results

3.3.1. Temperature and voltage distribution in Au nanosheet devices. Figure 7(a) shows the cross-sectional schematic of the Au nanosheet device assumed in this calculation. The Au nanosheet and the intermediate electrodes with the thicknesses $t_{ch} = t_{int} = 18$ nm were formed on the Si substrate with the 1 μm thick SiO_2 film, and the drain and source electrodes were in contact with the intermediate electrodes. The entire Si substrate was assumed to be at $T_0 = 25$ °C. The drain voltage V_D was applied to the drain electrode, and the source electrode was grounded. The volteges V_{int} and V_{ch} were voltage drops in the intermediate electrode region and in the channel region, respectively. Figure 7(b) shows the relationship between κ_{int} and the power required to raise the channel edge temperature to 200 °C in the Au nanosheet with $W_{ch} = 400$ nm and $L_{ch} = 2$ μm. The power consumption had a minimum value at $\kappa_{int} = 75\ \mathrm{W \cdot m^{-1} \cdot K^{-1}}$, indicating that there is an optimal κ_{int} to raise the entire channel above a certain temperature with lowest power consumption. As will be discussed in the Sect. 3.3.3, the optimal κ_{int} depends on L_{ch}. Figures 7(c)–7(e) present the temperature profiles of the Au nanosheet devices with κ_{int} of 318, 70, and $15\ \mathrm{W \cdot m^{-1} \cdot K^{-1}}$. Thermal localization within the Au nanosheet channel was achieved when using lower κ_{int}, thus reducing the temperature gradient in the channel. This trend is consistent with the simulation result shown in Fig. 5(b). In addition, when lower κ_{int} materials were used, the thermal localization was achieved with shorter L_{int}, thus reducing the size of the intermediate electrodes, as shown with gray backgrounds in Figs. 7(c)–7(e). Figures 7(f)–7(h) present the normalized voltage profiles in the same devices in Figs. 7(c)–7(e). Here, V_D $(=V_{ch} + 2V_{int})$ was normalized by V_{ch}. In these voltage profiles, we did not take into account the semi-elliptical structure of the intermediate electrodes and the voltage distribution due to the temperature gradient inside the channel and the intermediate electrodes, and we simplified these voltage profiles by assuming that V_{ch} and V_{int} were uniformly applied to L_{ch} and L_{int}, respectively. Figures 7(f)–7(h) indicated that R_{int} increased as κ_{int} decreased despite the L_{int} reduction, and the voltage drop in the intermediate electrode region became larger. Therefore, the dependence of power consumption on κ_{int} in Fig. 7(b) can be interpreted as follows: when κ_{int} was small, the larger R_{int} than R_{ch} caused the

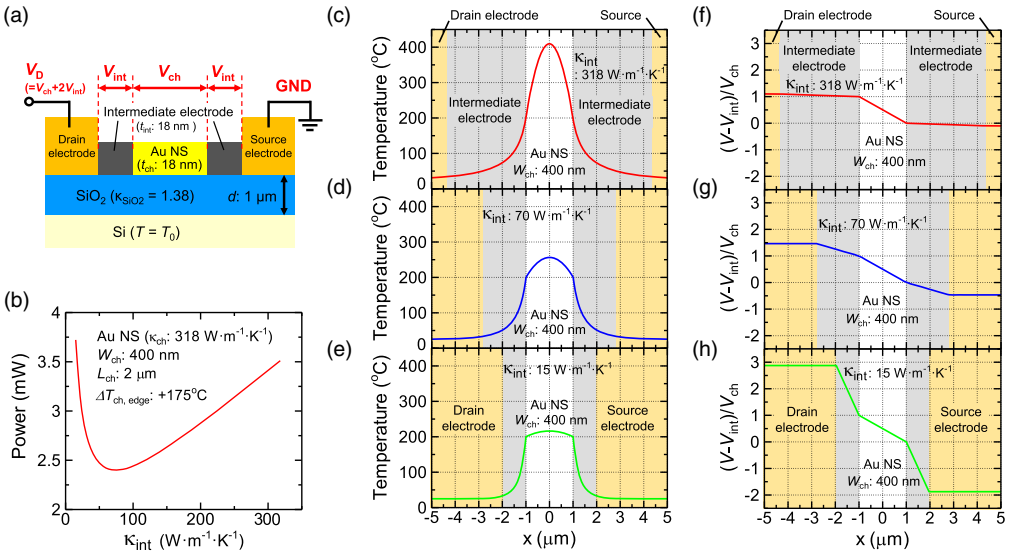

Fig. 7. (a) Cross-sectional schematic of the Au nanosheet device assumed in this calculation. The voltages applied to each region of the device are also shown. (b) Relationship between thermal conductivity of the intermediate electrode κ_{int} and the power required to raise the channel edge temperature to 200 °C in the Au nanosheet with $W_{ch} = 400$ nm and $L_{ch} = 2$ μm. (c)–(e) Temperature profiles of the devices and (f)–(h) normalized voltage profiles with different κ_{int}. (c), (f) κ_{int}: 318 W · m^{-1} · K^{-1}, (d), (g) κ_{int}: 70 W · m^{-1} · K^{-1}, (e), (h) κ_{int}: 15 W · m^{-1} · K^{-1}. Intermediate electrode regions are shown with gray backgrounds, and drain and source electrode regions are shown with yellow backgrounds.

increase of power consumption. On the other hand, when κ_{int} was large, the lower thermal resistance of the intermediate electrode $\mathcal{R}_{int}$ than that of the substrate $\mathcal{R}_{sub}$ caused the heat dissipation from the channel to the intermediate electrodes, resulting in the larger temperature gradient inside the channel and the increase of power consumption.[35] We expect from this result that it is preferable that the heat dissipations to the intermediate electrodes and to the substrate are comparable in order to reduce the temperature gradient and minimize the power consumption. As noted in the Calculation conditions (v), σ_{int} and κ_{int} are correlated by the Wiedemann–Franz law, making it impossible to design the electrical and thermal properties of the intermediate electrodes separately. Thus, their optimal values exist depending on the device as shown in Fig. 7(b), and the electrode material should be properly selected.

3.3.2. Relationship between κ_{int} and the power consumption of the Au nanosheet device with the fixed channel aspect ratio (CAR). Next, we investigated the influence of the channel width W_{ch} on the power consumption. Figure 8(a) shows the relationship between κ_{int} and the power consumption in the Au nanosheet devices with the fixed channel aspect ratio (CAR) of W_{ch}:$L_{ch} = 1$:5. Here, the result shown by the red line (W_{ch}:400 nm) is identical to that in Fig. 7(b). The energetically optimal κ_{int} decreased as the channel size decreased for the device structures with the same CAR. We considered that, since the heat dissipation to the substrate (inversely proportional to the thermal resistance of the substrate $\mathcal{R}_{sub}$) decreased as W_{ch} decreased, it was preferable to also decrease the heat dissipation to the intermediate electrode (inversely proportional to the thermal resistance of the intermediate electrode $\mathcal{R}_{int}$) and to balance these two heat dissipation components for minimizing the power consumption in the smaller channel.[35] Figure 8(b) presents the relationship between κ_{int} and the sensor response degradation rate r when the CAR is W_{ch}:$L_{ch} = 1$:5. Here, the response degradation rate is defined as $r = R_{ch}/(R_{ch} + 2R_{int})$. This means that only R_{ch} changes in the sensing stage (Response $= \Delta R_{ch}/(R_{ch} + 2R_{int})$), indicating that the response decreases as R_{int} increases. The dots on the each line in Fig. 8(b) indicate the locations κ_{int} which minimizes the power consumption obtained in Fig. 8(a). This result

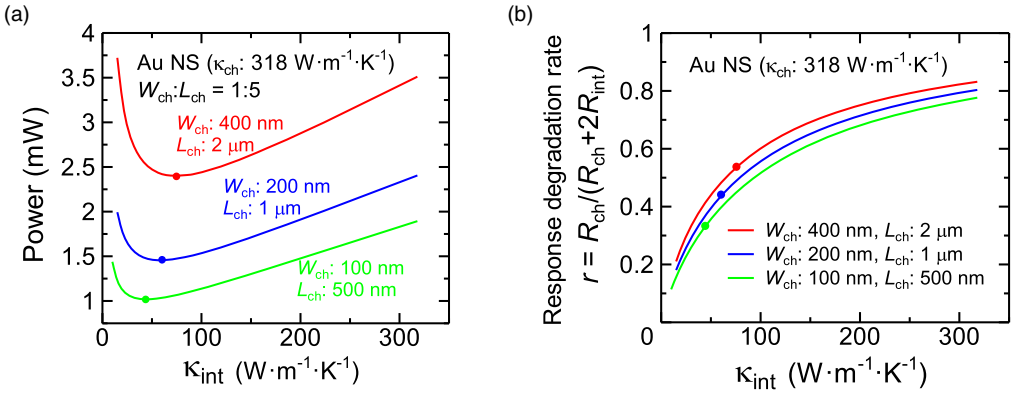

Fig. 8. (a) Relationship between κ_{int} and the power consumption of the Au nanosheet device with the fixed CAR of W_{ch}:$L_{ch} = 1$:5. (b) Relationship between κ_{int} and the response degradation rate $r = R_{ch}/(R_{ch} + 2R_{int})$. Red line: W_{ch}:400 nm, blue line: W_{ch}:200 nm, green line: W_{ch}:100 nm.

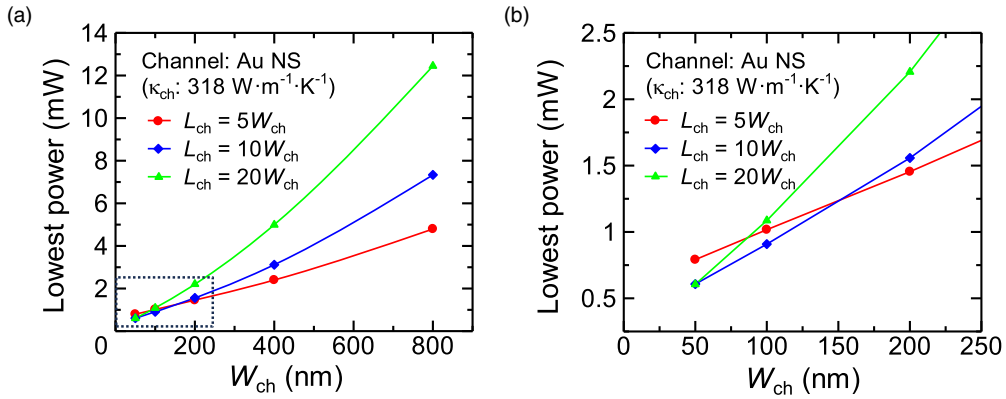

Fig. 9. (a) Relationship between W_{ch} and the minimum power for different CAR. Red line: $L_{ch} = 5W_{ch}$, blue line: $L_{ch} = 10W_{ch}$, green line: $L_{ch} = 20W_{ch}$. (b) Enlarged view of the region in (a) where W_{ch} is less than 200 nm.

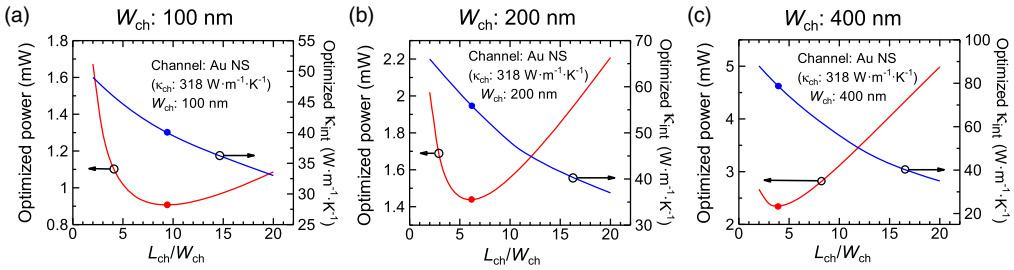

Fig. 10. (a)–(c) CAR dependence of the minimized power and optimized κ_{int}. (a) W_{ch}:100 nm, (b) W_{ch}:200 nm, (c) W_{ch}:400 nm.

exhibited that, when the optimal κ_{int} were applied for each device with a fixed CAR, the sensor response decreased as W_{ch} decreased though the power consumption decreased.

3.3.3. Minimum power consumption of Au nanosheet with various W_{ch} and L_{ch}. Figures 9(a) and 9(b) show the W_{ch} dependence of the power consumption for the different CAR: W_{ch}:L_{ch} = 1:5 (red line), 1:10 (blue line), 1:20 (green line), respectively. The power consumption increased as W_{ch} increased when the CAR was fixed. In addition, when W_{ch} was large (i.e. $W_{ch} = 800$ nm), the power consumption increased as L_{ch} increased as shown in Fig. 9(a). However, when W_{ch} was less than 200 nm in Fig. 9(b), the power consumption was smaller for W_{ch}:L_{ch} = 1:10 than for 1:5. Hence, we can expect that there are the energetically most optimal L_{ch} and κ_{int} depending on W_{ch}.

Then, we further investigated the CAR dependence of the minimized power and the optimized κ_{int} as shown in Figs. 10(a)–10(c). Here, κ_{int} that minimizes the power consumption and its optimized power are plotted for each CAR (L_{ch}/W_{ch}). These results clearly demonstrated that there was the optimal CAR depending on W_{ch}, and the optimal CAR decreased as W_{ch} became larger. Furthermore, the energetically optimal κ_{int} decreased as L_{ch} became longer for the fixed W_{ch}. For the longer L_{ch}, the temperature gradient near the center of the channel decreases, and the heat dissipation to the substrate becomes dominant in that region. In this case, we considered that it is energetically more favorable for raising the entire channel temperature to suppress the heat dissipation from the channel edge to the intermediate electrode.

3.3.4. Response degradation rate of Au nanosheet devices. From R_{ch} and R_{int} obtained from the result in Figs. 10(a)–10(c), we plotted the relationship between L_{ch}/W_{ch} and r, as shown in Fig. 11. R_{ch} increased and it

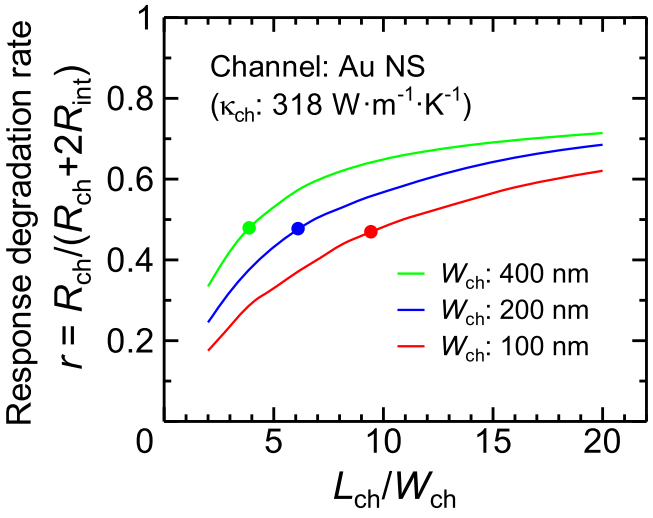

Fig. 11. Relationship between the CAR L_{ch}/W_{ch} and response degradation rate r for the fixed W_{ch}.

became dominant over R_{int} as L_{ch} became longer, thus lowering r. The dots on the each line in Fig. 11 indicate the locations that minimizes the power consumption for each W_{ch} in Figs. 10(a)–10(c). For all W_{ch}, r was approximately 0.5 (R_{ch}:$2R_{int}$ = 1:1) when the optimal L_{ch} and κ_{int} that minimized the power consumption were chosen. These results from Figs. 8 to 11 suggest that it is necessary to consider both the balance between R_{ch} and R_{int} ($R_{ch} \simeq 2R_{int}$) and the balance between $\mathcal{R}_{sub}$ and $\mathcal{R}_{int}$ ($\mathcal{R}_{sub} \simeq \frac{1}{2}\mathcal{R}_{int}$) in order to minimize the power consumption of the Joule-heated metal nanosheet, as discussed in the Sect. 3.3.2.

3.4. Optimization strategy for device structure

In this section, we will verify the validity of the above consideration about the electrical and thermal resistances, and

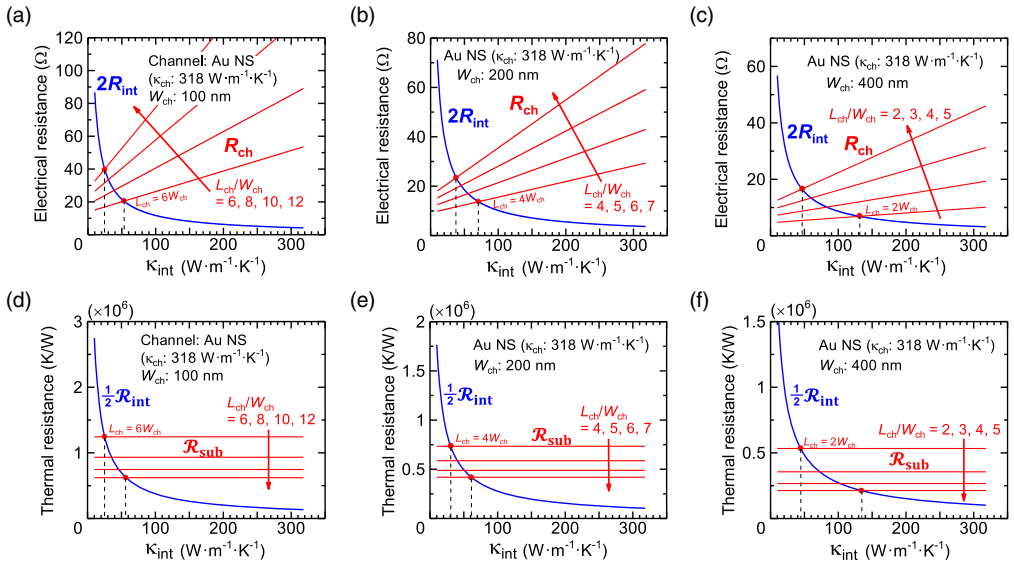

Fig. 12. (a)–(c) κ_{int} dependences of R_{ch} (red lines) and R_{int} (blue lines) for various W_{ch}. (d)–(f) κ_{int} dependences of $\mathcal{R}_{sub}$ (red lines) and $\mathcal{R}_{int}$ (blue lines). (a), (d) W_{ch}:100 nm, (b), (e) W_{ch}:200 nm, (c), (f) W_{ch}:400 nm.

then, we will describe the optimization strategy of the device structure.

3.4.1. Parameters of electrical and thermal resistances. When fabricating a metal nanosheet gas sensor, the metal material used for the channel is first determined according to the molecular species (target gas) to be detected (e.g. Au for H_2S, Pt for H_2). Next, the substrate material and its thickness are second determined according to the device on which the sensor is mounted. Lastly, the technically feasible channel width W_{ch} is determined to integrate the sensors. Thus, the electrical and thermal conductivities of the channel σ_{ch} and κ_{ch}, the channel width W_{ch}, the thermal conductivity of the substrate κ_{sub}, and its thickness t_{sub} are assumed to be fixed, and the channel length L_{ch} and the thermal conductivity of the intermediate electrode κ_{int} are variables for optimizing the device structure.

Here, we consider the variables that R_{ch}, R_{int}, $\mathcal{R}_{sub}$, and $\mathcal{R}_{int}$ are functions of. Firstly, since R_{ch} is expressed as Eq. (6), R_{ch} is the function of L_{ch}. In addition, because the temperature distribution in the channel depends on κ_{int}, R_{ch} is the function of κ_{int}. Second, since R_{int} is expressed as Eq. (8) and ρ_{int} depends on κ_{int}, R_{int} is the function of κ_{int}. Third, $\mathcal{R}_{sub}$ in a two-dimensional heat diffusion system can be approximated by the following equation:[36)]

$$\mathcal{R}_{sub} = \frac{\ln(8d/\pi W_{ch})}{\pi \kappa_{sub} L_{ch}}. \tag{9}$$

Hence, $\mathcal{R}_{sub}$ is the function of L_{ch}. Lastly, considering $\mathcal{R}_{int}$ as the analogy of R_{int} in Eq. (8), $\mathcal{R}_{int}$ can be written as follows:

$$\mathcal{R}_{int} = \frac{1}{\kappa_{int}} \cdot \frac{1}{\pi t_{int}} \log\left(\frac{\sqrt{W_{ch}^2/4 + L_H^2} + L_H}{W_{ch}/2} \right). \tag{10}$$

From this equation, $\mathcal{R}_{int}$ is the function of κ_{int}. Note that the thermal resistance of the substrate under the intermediate electrode ($\mathcal{R}_{sub}^{int}$) is not taken into account for simplicity. In summary, R_{int} and $\mathcal{R}_{int}$ decreases as κ_{int} increases from Eqs. (8) and (10). On the other hand, R_{ch} and $\mathcal{R}_{sub}$ are the function of L_{ch}, and R_{ch} increases as L_{ch} increases [Eq. (6)], while $\mathcal{R}_{sub}$ decreases [Eq. (9)]. That is, the L_{ch} dependences of R_{ch} and $\mathcal{R}_{sub}$ show the opposite trends. This indicates that there are specific κ_{int} values which achieve both the balance of the electrical resistances ($R_{ch} = 2R_{int}$) and the balance of the thermal resistances ($\mathcal{R}_{sub} = \frac{1}{2}\mathcal{R}_{int}$). Once the optimal κ_{int} values are determined, the optimal L_{ch} values are also determined.

3.4.2. Estimation of optimal device structure from electrical and thermal resistances. Figures 12(a)–12(c) show the κ_{int} dependences of R_{ch} (red lines) and R_{int} (blue lines) for various W_{ch} (100 nm, 200 nm, 400 nm), and Figs. 12(d)–12(f) show those of $\mathcal{R}_{sub}$ (red lines) and $\mathcal{R}_{int}$ (blue lines). Here, the relationships between L_{int} and κ_{int}, ΔT_{int} and κ_{int}, ΔT_{ch} and κ_{int}, and $\Delta T_{ch,\,ave}$ and L_{ch}/W_{ch} were required for the calculations. These relationships were all derived by the fitting from the results obtained in Figs. 7–11.

In Figs. 12(a)–12(c), the balance between the electrical resistances ($R_{ch} \simeq 2R_{int}$) is achieved at the optimal L_{ch}/W_{ch} and κ_{int} which are obtained from Fig. 10. Applying these L_{ch}/W_{ch} and κ_{int} to the thermal resistances in Figs. 12(d)–12(f), we confirmed $\mathcal{R}_{sub} \simeq \frac{1}{2}\mathcal{R}_{int}$. Thus, we demonstrated that the balance between $\mathcal{R}_{sub}$ and $\mathcal{R}_{int}$ should also be achieved in order to optimize the device structure. Specifically, in Figs. 12(c) and 12(f), these two balances were achieved when L_{ch}/W_{ch} was 3–4 and κ_{int} was 70–80 $\mathrm{W \cdot m^{-1} \cdot K^{-1}}$. These results were approximately in good agreement with κ_{int} and L_{ch} in Fig. 10(c), where the power consumption was minimum in the Au nanosheet device with W_{ch} of 400 nm. The balanced L_{ch}/W_{ch} and κ_{int} for W_{ch} of 100 nm and 200 nm in Figs. 12(a), 12(d) and 12(b), 12(e) were also approximately consistent with the results in Figs. 10(a) and 10(b), respectively. Although the thermal resistance of the substrate under the intermediate electrode ($\mathcal{R}_{sub}^{int}$) was not considered in this study, the estimation was still reasonable.

From these results, we concluded that the metal nanosheet device structures that enables Joule heating of the entire channel with minimum power are L_{ch} and κ_{int} such that both

the balance of the electrical resistances ($R_{ch} \simeq 2R_{int}$) and the balance of the thermal resistances ($\mathcal{R}_{sub} \simeq \frac{1}{2}\mathcal{R}_{int}$) are achieved. These optimal L_{ch} and κ_{int} can be approximately found by plotting the κ_{int} dependences of the electrical resistances and the thermal resistances, as shown in Figs. 12(a)–12(f). The same design strategy can be applied to the case where a metal other than Au is used as the channel material. For example, when Pt, which has lower electrical and thermal conductivities than Au, is used as the channel material, the κ_{int} and σ_{int} of the optimal intermediate electrode are also expected to be lower, and their optimal values can be estimated using the above strategy.

In actual device fabrication, alloys may be used to achieve the desired κ_{int} material. In Au–Pt alloys, for example, a small amount of Pt added to Au has yieleded alloys with a wide range of thermal conductivity below that of Au (κ: 318 $W \cdot m^{-1} \cdot K^{-1}$).[37] Furthermore, various alloys that follow the Wiedemann–Franz law and are below the thermal conductivity of Pt ((κ: 71 $W \cdot m^{-1} \cdot K^{-1}$)) have been obtained in Pt–nickel (Ni) alloys and Pt–vanadium (V) alloys.[38] Therefore, we expect that the desired intermediate electrodes can be achieved by using single metals or alloys.

4. Conclusions

We demonstrated the Au nanosheet H_2S sensors operated with Joule heating for low-power operation. In the Joule-heated Au nanosheet sensor with the Au electrodes, the large heat dissipation to the electrodes caused the insufficient heating around the channel edges, resulting in the lower responses and recovery characteristics than the Au nanosheet sensors heated by the external heater. To localize the Joule heat within the channel, we used Pt, which has lower thermal conductivity than Au, as the electrode material to suppress the heat dissipation to the electrodes, resulting in the lower power consumption and faster recovery speed. Since it was experimentally confirmed that the use of a material having lower thermal conductivity than the channel metal for the electrode contributes to the lower power consumption of the Joule-heated metal nanosheet sensors, we then discussed the optimal sensor structure and the material characteristics for its electrode by developing the analytical model. Based on Hunley's analytical model for calculating temperature distribution in the Joule-heated metal nanosheet, we calculated the power consumption required to raise the entire channel temperature to the certain temperature by introducing the structure of the intermediate electrodes. As a result, we confirmed that the optimal channel length L_{ch} and the optimal thermal conductivity of the intermediate electrode κ_{int} that made the power consumption minimum varied with the channel width W_{ch}. We also confirmed that the electrical resistances of the channel R_{ch} and the intermediate electrode (R_{int}) were of the similar values ($R_{ch} \sim 2R_{int}$) when L_{ch} and κ_{int} were optimal for every W_{ch}. Finally, we discussed the thermal resistances of the metal nanosheet, namely, the thermal resistance of the substrate $\mathcal{R}_{sub}$ and that of the intermediate electrode ($\mathcal{R}_{int}$). We confirmed that the metal nanosheet device structures that enables Joule heating of the entire channel with minimum power are L_{ch} and κ_{int} such that both the balance of the electrical resistances ($R_{ch} \simeq 2R_{int}$) and the balance of the thermal resistances ($\mathcal{R}_{sub} \simeq \frac{1}{2}\mathcal{R}_{int}$)are achieved. We also confirmed that, when designing the metal nanosheet sensor, the optimal L_{ch} and κ_{int} can be approximately estimated by plotting the κ_{int} dependences of the electrical resistances (R_{ch}, R_{int}) and the thermal resistances ($\mathcal{R}_{sub}$, $\mathcal{R}_{int}$). Because our analytical model is based on the Wiedemann–Franz law, it is applicable for all the metal nanosheet sensors.

Acknowledgments

This work was partly supported by a JST CREST Grant No. JPMJCR19I2 and JPMJCR22C4, JST COI-NEXT Grant No. JPMJPF2202, and JSPS KAKENHI Grant Nos. 22KJ0891, 19H00756, 18H05423.

Appendix A: Potential formed by elliptical cylinder conductors

First, we consider the potential of a cylindrical conductor with an elliptical cross-section of semi-axes a and b ($a > b$) when a charge density of λ per unit length is distributed on its surface, as shown in Fig. A·1.

When comparing the real and imaginary parts of the complex function $z = A\cos w$, where $z = x + iy$ and $w = u + iv$, we obtain the following expressions:

$$x = A\cosh v\cos u, \quad y = -A\sinh v\sin u. \tag{A·1}$$

As a result, we can express the following relationships:

$$\frac{x^2}{A^2\cosh^2 v} + \frac{y^2}{A^2\sinh^2 v} = 1 \tag{A·2}$$

$$\frac{x^2}{A^2\cos^2 u} - \frac{y^2}{A^2\sin^2 u} = 1. \tag{A·3}$$

When $v = v_0$, let $A\cosh v_0 = a$ and $A\sinh v_0 = b$. Using Eq. (A·2), we have:

$$\frac{x^2}{a^2} + \frac{y^2}{b^2} = 1, \quad A = \sqrt{a^2 - b^2}. \tag{A·4}$$

This equation represents the ellipse equation on the surface of the conductor. Therefore, the surfaces with constant v correspond to equipotential surfaces, and the imaginary part v of w represents a electric potential.

In this case

$$w = \cos^{-1}\left(\frac{z}{\sqrt{a^2 - b^2}}\right). \tag{A·5}$$

This corresponds to the case of providing a charge of $2\pi\varepsilon_0$ per unit length. Therefore, when providing a charge of λ per unit length, we have:

$$w = \frac{\lambda}{2\pi\varepsilon_0}\cos^{-1}\left(\frac{z}{\sqrt{a^2 - b^2}}\right). \tag{A·6}$$

The imaginary part of Eq. (A·6) determines the potential. In this case, the equation corresponding to Eq. (A·2) becomes as follows:

$$\frac{x^2}{A^2\cosh^2(v \cdot 2\pi\varepsilon_0/\lambda)} + \frac{y^2}{A^2\sinh^2(v \cdot 2\pi\varepsilon_0/\lambda)} = 1,$$
$$A = \sqrt{a^2 - b^2}. \tag{A·7}$$

In the equipotential surfaces, where v is constant, and denoting $A\cosh(v \cdot 2\pi\varepsilon_0/\lambda) = a'$ and $A\sinh(v \cdot 2\pi\varepsilon_0/\lambda) = b'$, we

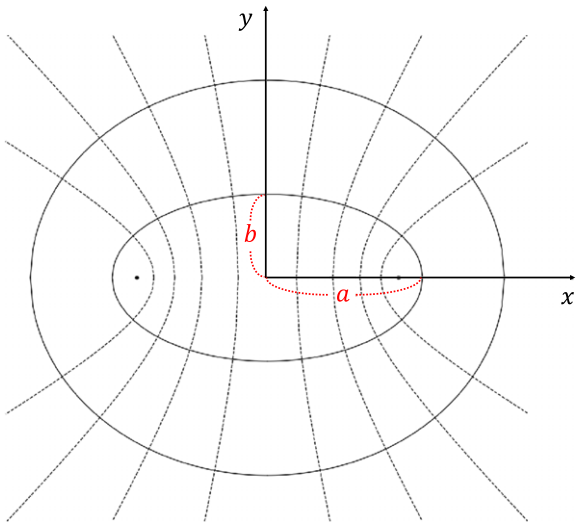

Fig. A·1. Equipotential surfaces and electrical flux lines of conducting elliptical cylinder.

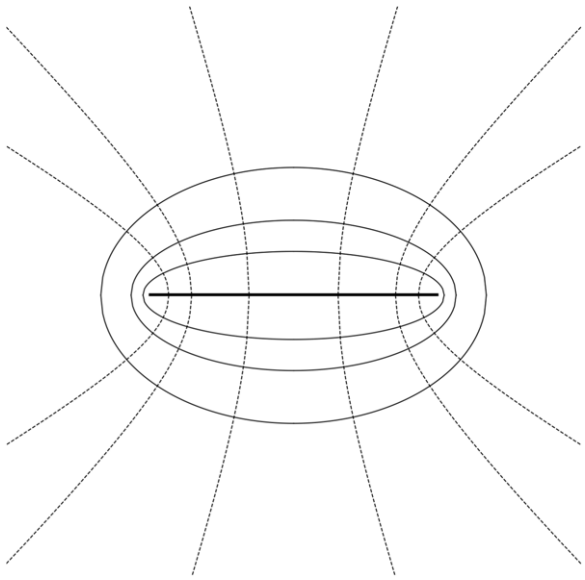

Fig. A·2. Equipotentials and electrical flux lines of conductive thin plate.

have:

$$\frac{x^2}{a'^2}+\frac{y^2}{b'^2}=1,\quad \sqrt{a'^2-b'^2}=A=\sqrt{a^2-b^2}. \tag{A·8}$$

These are confocal ellipses with semi-axes a' and b'. Consequently, the equipotential surfaces correspond to cylindrical surfaces where the cross-sections are described by the confocal ellipse equation given in Eq. (A·8). The electric potential v of the cylindrical surface, where the semi-axes of the cross-sectional ellipses are a' and b', can be found by solving for b' in terms of v using the equation:

$$v=\frac{\lambda}{2\pi\varepsilon_0}\sinh^{-1}\frac{b'}{\sqrt{a'^2-b'^2}}\quad(\sqrt{a'^2-b'^2}=\sqrt{a^2-b^2}). \tag{A·9}$$

The electrical flux lines are represented by curves with constant u. The corresponding equation to Eq. (A·3) is:

$$\frac{x^2}{A^2\cos^2(u\cdot 2\pi\varepsilon_0/\lambda)}-\frac{y^2}{A^2\sin^2(u\cdot 2\pi\varepsilon_0/\lambda)}=1 \tag{A·10}$$

Denoting $A\cos(u\cdot 2\pi\varepsilon_0/\lambda)=a_1$ and $A\sin(u\cdot 2\pi\varepsilon_0/\lambda)=b_1$, we have:

$$\frac{x^2}{a_1^2}-\frac{y^2}{b_1^2}=1,\quad a_1^2+b_1^2=A^2=a^2-b^2. \tag{A·11}$$

These equations represent a set of confocal hyperbolas, which represent the electrical flux lines.

Next, let us consider the case where a thin conductor plate with a width of $2a$ is charged with a linear charge density λ, as shown in Fig. A·2. In this case, the thin plate can be approximated as having an elliptical shape with the long axis being $2a$ and the short axis approaching $2b\to 0$ in the limit. Therefore, based on Eq. (A·6), the electric potential is given by:

$$w=\frac{\lambda}{2\pi\varepsilon_0}\cos^{-1}\left(\frac{z}{a}\right), \tag{A·12}$$

where v is the imaginary part of w. The equipotential surfaces have cross-sections described by the equation:

$$\frac{x^2}{a'^2}+\frac{y^2}{b'^2}=1,\quad \sqrt{a'^2-b'^2}=a. \tag{A·13}$$

These cross-sections form a set of confocal ellipses, which represent the equipotential surfaces.

As a result, the equipotential surfaces originating from the edge of the nanosheet channel are semi-elliptical in shape.

Appendix B: Capacity between two elliptical conductors

Based on the above discussion in Appendix A, we will calculate the capacitance per unit length of a cylindrical capacitor with inner and outer tubes, where the cross-sections of both tubes are ellipses with semi-axes a_1, b_1:($a_1>b_1$) and a_2, b_2:($a_2>b_2$:$a_1<a_2$:$b_1<b_2$), respectively [Fig. B·1].

According to Eq. (A·9), let the potentials of the inner and outer tubes be denoted as V_1 and V_2, respectively:

$$V_1=\frac{\lambda}{2\pi\varepsilon_0}\sinh^{-1}\frac{b_1}{\sqrt{a_1^2-b_1^2}},\quad V_2=\frac{\lambda}{2\pi\varepsilon_0}\sinh^{-1}\frac{b_2}{\sqrt{a_2^2-b_2^2}}. \tag{B·1}$$

Therefore, the potential difference V_1-V_2 is:

$$\begin{aligned}V_1-V_2&=\frac{\lambda}{2\pi\varepsilon_0}\left\{\sinh^{-1}\frac{b_1}{\sqrt{a_1^2-b_1^2}}-\sinh^{-1}\frac{b_2}{\sqrt{a_2^2-b_2^2}}\right\}\\&=\frac{\lambda}{2\pi\varepsilon_0}\log\sqrt{\frac{a_1+b_1}{a_1-b_1}\frac{a_2-b_2}{a_2+b_2}}\\&=\frac{\lambda}{2\pi\varepsilon_0}\log\frac{a_1+b_1}{a_2+b_2}\quad(\because\sqrt{a_1^2-b_1^2}=\sqrt{a_2^2-b_2^2}).\end{aligned} \tag{B·2}$$

Therefore, the capacitance per unit length C is:

$$C=\frac{\lambda}{V_1-V_2}=2\pi\varepsilon_0/\log\frac{a_1+b_1}{a_2+b_2}. \tag{B·3}$$

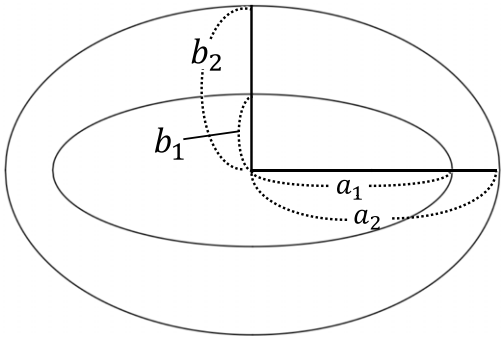

Fig. B·1. Two confocal ellipses with semi-axes a_1, b_1 and a_2, b_2.

This represents the capacitance per unit length of the cylindrical capacitor with inner and outer tubes.

ORCID iDs

Ken Uchida https://orcid.org/0000-0001-8307-5232

1) I. Darmadi, F. A. A. Nugroho, and C. Langhammer, ACS Sens. **5**, 3306 (2020).
2) O. Lupan, N. Magariu, D. Santos-Carballal, N. Ababii, J. Offermann, P. Pooker, S. Hansen, L. Siebert, N. H. de Leeuw, and R. Adelung, ACS Appl. Mater. Interfaces **15**, 27340 (2023).
3) A. T. Güntner, S. Abegg, K. Königstein, P. A. Gerber, A. Schmidt-Trucksäss, and S. E. Pratsinis, ACS Sens. **4**, 268 (2019).
4) S. Emam, M. Nasrollahpour, B. Solarusso, X. Cai, S. Grant, P. Kulkarni, A. Ekenseair, C. Gharagouzloo, C. F. Ferris, and N. X. Sun, Alzheimer's Dementia: Diagnosis, Assessment Disease Monitoring **12**, e12088 (2020).
5) K. Mahmodi, M. Mostafaei, and E. Mirzaee-Ghaleh, Fuel **258**, 116114 (2019).
6) A. Vij, S. Vijendra, A. Jain, S. Bajaj, A. Bassi, and A. Sharma, Proc. Comput. Sci. **167**, 1250 (2020).
7) Z. Li et al., Mater. Horiz. **6**, 470 (2019).
8) H. Yin, Z. Mu, H. Li, X. Liu, and A. J. Mason, IEEE Sens. J. **18**, 7899 (2018).
9) Z. Li, N. Wang, Z. Lin, J. Wang, W. Liu, K. Sun, Y. Q. Fu, and Z. Wang, ACS Appl. Mater. Interfaces **8**, 20962 (2016).
10) H. He, C. Zhao, J. Xu, K. Qu, Z. Jiang, Z. Gao, and Y. Y. Song, ACS Sens. **6**, 3387 (2021).
11) H. Li, X. Mu, Y. Yang, and A. J. Mason, IEEE Sens. J. **14**, 3391 (2014).
12) T. Tanaka, Y. Hamanaka, T. Kato, and K. Uchida, ACS Sens. **7**, 716 (2022).
13) C. Fàbrega, O. Casals, F. Hernández-Ramirez, and J. D. Prades, Sens. Actuators B **256**, 797 (2018).
14) J. S. Lee, K. W. Choi, J. Y. Yoo, M. S. Jo, and J. B. Yoon, Small **16**, 1906845 (2020).
15) K. Chikkadi, M. Muoth, V. Maiwald, C. Roman, and C. Hierold, Appl. Phys. Lett. **103**, 223109 (2013).
16) T. Yokoyama, T. Tanaka, Y. Shimokawa, R. Yamachi, Y. Saito, and K. Uchida, ACS Appl. Nano Mater. **1**, 3886 (2018).
17) Y. H. Kim, S. J. Kim, Y. J. Kim, Y. S. Shim, S. Y. Kim, B. H. Hong, and H. W. Jang, ACS Nano **9**, 10453 (2015).
18) P. Offermans, H. D. Tong, J. M. van Rijn, P. Merken, S. H. Brongersma, and M. Crego-Calama, Appl. Phys. Lett. **94**, 223110 (2009).
19) N. J. Humphrey, E. J. Choi, N. P. Drago, J. C. Hemminger, and R. M. Penner, ACS Sens. **8**, 2869 (2023).
20) T. Tanaka et al., IEEE Trans. Electron Devices **66**, 5393 (2019).
21) T. Tanaka, S. Hoshino, T. Takahashi, and K. Uchida, Sens. Actuators B **258**, 913 (2018).
22) R. G. Tobin, Surf. Sci. **502-503**, 374 (2002).
23) T. Kato, T. Tanaka, T. Yajima, and K. Uchida, Jpn. J. Appl. Phys. **60**, SBBH13 (2021).
24) K. S. Yoo, I. W. Sorensen, and W. S. Glaunsinger, J. Vac. Sci. Technol. **12**, 192 (1994).
25) T. Kato, T. Tanaka, H. Miyagishi, J. Terao, and K. Uchida, Ext. Abstr. Electron Devices Technology and Manufacturing Conf., 2023.
26) S. D. Sawtelle and M. A. Reed, Phys. Rev. B **99**, 054304 (2019).
27) R. Hoffmann, D. Weissenberger, J. Hawecker, and D. Stöffler, Appl. Phys. Lett. **93**, 043118 (2008).
28) C. Durkan, M. A. Schneider, and M. E. Welland, J. Appl. Phys. **86**, 1280 (1999).
29) C. Durkan and M. E. Welland, Ultramicroscopy **82**, 125 (2000).
30) T. Kato, T. Tanaka, T. Yajima, and K. Uchida, Ext. Abstr. Solid State Devices and Materials, 2023 p. 19.
31) D. P. Hunley, S. L. Johnson, R. L. Flores, A. Sundararajan, and D. R. Strachan, J. Appl. Phys. **113**, 234306 (2013).
32) R. Holm, *Electric Contacts: Theory and Application* (Springer, Berlin, 1967).
33) A. Jain and A. J. H. McGaughey, Phys. Rev. B **93**, 081206(R) (2016).
34) Y. Wang, Z. Lu, and X. Ruan, J. Appl. Phys. **119**, 225109 (2016).
35) E. Pop, Nanotechnology **19**, 295202 (2008).
36) F. P. Incropera, D. P. Dewitt, T. L. Bergman, and A. S. Lavine, *Fundamentals of Heat and Mass Transfer* (Wiley, New York, 2006) 6th ed..
37) A. S. Darling, Platinum Metals Rev. **6**, 106 (1962).
38) Y. Terada, K. Ohkubo, and T. Mohri, Platinum Metals Rev. **49**, 21 (2005).